nature communications

Article

https://doi.org/10.1038/s41467-025-63390-6

Versatile polymer-coated Ag_2Se thermoelectric materials and devices for multi-scenario applications developed by direct-ink printing

Received: 27 September 2024

Accepted: 19 August 2025

Published online: 26 September 2025

Check for updates

Jie Qin[1], Yong Du[1] ✉, Qiufeng Meng[1], Song Chen[2], Min Hong[3] ✉ & Qinfei Ke[1] ✉

Flexible thermoelectrics offer eco-friendly solutions for wearable health monitoring, smart sensors, and energy harvesting. However, challenges remain in device fabrication and performance enhancement. Herein, flexible thermoelectric films—Ag_2Se/methylcellulose, poly(3,4-ethylenedioxythiophene):poly(styrenesulfonate)@Ag_2Se/methylcellulose, and polyvinylpyrrolidone@Ag_2Se/methylcellulose—are fabricated via a scalable and economical direct-ink printing method. After cold pressing and annealing, the polyvinylpyrrolidone@Ag_2Se/methylcellulose film shows a record-high power factor of 2191.5 $\mu Wm^{-1}K^{-2}$ at 400 K among all the flexible organic/inorganic films prepared via direct-ink printing. The heterointerfaces, pores, boundaries, and dislocations formed in the composite films through the fabrication procedure are beneficial for enhancing the Seebeck coefficient and electrical conductivity simultaneously, as well as reducing the thermal conductivity. Three-leg flexible thermoelectric generators are fabricated using a direct-ink printing process, yielding a power density of 22.1 W/m^2 at a ΔT of 36.1 K. Such devices have been applied across various scenarios, including low-grade heat recovery, position identification, light-heat-electricity conversion, and respiratory monitoring. The direct-ink printing and thermoelectric performance optimization strategies have universal applicability, exhibiting potential for advancing flexible wearable electronics.

The rapid advancement of technologies such as artificial intelligence and 5 G has increased the interest in smart wearable devices[1,2]. However, traditional power supplies, such as lithium cells and nickel-zinc batteries, demand frequent recharging and/or replacement, which limits the long-term service of wearable devices. Flexible thermoelectric generators (f-TEGs) are gaining prominence because of their portability, light weight, eco-friendliness, rapid responsiveness, and high reliability[3]. f-TEGs can directly convert low-grade waste heat from non-planar sources (e.g., human skin and cylindrical pipes), as well as sunlight, into electrical power[4,5]. This capability enables them to demonstrate promising applications in energy harvesting, wearable health monitoring, and smart sensors. The efficiency of f-TEGs predominantly depends on the dimensionless figure of merit of TE materials ($ZT = S^2\sigma T/\kappa$, where S, σ, κ, and T are the Seebeck coefficient,

[1]School of Materials Science and Engineering, Shanghai Institute of Technology, Shanghai, China. [2]School of Materials Science and Engineering, Fujian University of Technology, Fuzhou, China. [3]Centre for Future Materials and School of Engineering, University of Southern Queensland, Springfield Central, Queensland, Australia. ✉e-mail: ydu@sit.edu.cn; min.hong@unisq.edu.au; kqf@sit.edu.cn

electrical conductivity, thermal conductivity, and absolute temperature, respectively)[6,7].

However, a major challenge in f-TEGs for wearable devices remains. Although inorganic TE materials always exhibit excellent TE properties, the lack of flexibility limits their practical application in f-TEGs. An ideal solution involves combining rigid inorganic materials with polymers to boost the flexibility without compromising their TE performance. Conducting polymers, such as poly(3,4-ethylenedioxythiophene):poly(styrenesulfonate) (PEDOT:PSS)[8], have been recognized as promising candidates for flexible TE materials, due to their inherently low κ and tunable σ; while insulating polymers, like polyvinylpyrrolidone (PVP)[9], primarily function as flexible low-κ matrices that facilitate the dispersion of inorganic TE materials, thereby showing certain potential as matrices for flexible TE composites. Thus, inorganic/polymer composites for f-TEGs have gained increasing attention, for example, $Bi_{0.5}Sb_{1.5}Te_3$/PEDOT:PSS[10], Te/PEDOT:PSS[11], and SWCNT/PVP[12] composite films.

Ag_2Se, as a typical n-type TE semiconductor, has attracted considerable attention due to its environmental friendliness and outstanding performance near room temperature (RT)[13,14]. For example, Ding et al.[15] reported that through a sequential vacuum filtration and hot pressing process, the fabricated flexible Ag_2Se/nylon composite film achieved a power factor ($PF = S^2\sigma$) of 987.4 $\mu Wm^{-1} K^{-2}$ at 300 K. Jiang et al.[16] and Cai et al.[9] subsequently employed a similar approach to fabricate the flexible Ag_2Se film and PVP@Ag_2Se composite film, yielding a PF of 1882 $\mu Wm^{-1} K^{-2}$ and 1910 $\mu Wm^{-1} K^{-2}$ at RT, respectively. However, the complex and high-cost equipment needed for the vacuum hot-pressing technology, and the low design flexibility of the vacuum filtration process, pose significant challenges for the large-scale application of flexible TE composite films.

Direct-ink printing can print different types of slurries, which are composed of pure polymers, organic/inorganic composites, or pure inorganic materials, for the construction of the desired shapes layer by layer. The advantages of the direct-ink printing include simple operation, mass production, high design flexibility, and broad applicability[17]. More importantly, direct-ink printing through layer-by-layer assembly can control the thickness and configuration of printed materials, which is beneficial for enhancing the flexibility and TE performance, and therefore offers a more sustainable and efficient option for developing advanced flexible TE materials. Direct-ink printing can even fabricate f-TEGs directly, when compared with traditional material preparation processes, such as thermal co-evaporation[13], vacuum filtration[18], screen printing[19], and hot pressing process[15]. However, few studies on flexible Ag_2Se/polymer TE composite films have been reported via the direct-ink printing, and the corresponding composite films also exhibited relatively low TE performance, not to mention the f-TEGs directly printed via this technology.

In this study, we developed flexible polymer-coated Ag_2Se TE composite films and f-TEGs using direct-ink printing. Figure 1 shows a comprehensive flowchart of the PVP@Ag_2Se/MC composite films and prototypical f-TEGs. A critical aspect of this technology is the design and preparation of a slurry with a suitable viscosity. Methylcellulose (MC), a cellulose derivative, has many advantages, e.g., tunable viscosity, good film-forming capability, flexibility, non-toxicity, and affordability[20]; herein, it was used as a binder to prepare the slurry. A wet chemical method was applied to coat PEDOT:PSS or PVP onto the surfaces of Ag_2Se nanowires (NWs) to improve the dispersion ability of Ag_2Se NWs in the MC matrix. Subsequently, the direct-ink printing was employed to fabricate flexible TE films, and their TE properties were then optimized through a sequential cold pressing and annealing process. Furthermore, 3-leg f-TEGs were directly printed from the PVP@Ag_2Se/MC composite slurry, and their output performance was determined. The sensing and light-heat-electricity conversion capabilities of the f-TEGs were also systematically evaluated, confirming their significant potential for applications in low-grade heat recovery, position identification, light-heat-electricity conversion, respiratory monitoring, etc.

Results

Following the wet chemical synthesis and characterizations described in the Methods and Supplementary Information Note S1 and S2, Ag_2Se NWs, PEDOT:PSS-coated Ag_2Se NWs, and PVP-coated Ag_2Se NWs were synthesized. The improved dispersibility of PEDOT:PSS-coated Ag_2Se NWs and PVP-coated Ag_2Se NWs was shown in Fig. S1. With MC as a binder, slurries of Ag_2Se NWs/MC, PEDOT:PSS@Ag_2Se NWs/MC, and PVP@Ag_2Se NWs/MC were prepared for direct-ink printing of the corresponding films. Photographs in Fig. S2a–c illustrate the typical PVP@Ag_2Se/MC slurry (corresponding viscosity versus shear rate was shown in Fig. S3), and printed film before and after the annealing process, respectively. The printed pattern highlights the significant design freedom of the direct-ink printing (Fig. S2d).

Thermoelectric properties and analysis

Figure 2a–c depicted the temperature-dependent behavior of σ, S, and PF for Ag_2Se/MC, PEDOT:PSS@Ag_2Se/MC, and PVP@Ag_2Se/MC films (300–420 K). At 300 K, the σ of Ag_2Se/MC, PEDOT:PSS@Ag_2Se/MC, and PVP@Ag_2Se/MC films was 660.19 S/cm, 668.62 S/cm, and 753.92 S/cm, respectively (Fig. 2a). The σ gradually increased with rising temperature for all the films, and a σ of 1197.98 S/cm at 420 K was achieved for the PVP@Ag_2Se/MC film. According to Fig. 2b, all the films exhibited a negative S, confirming their n-type TE characteristics with electrons as the major charge carriers. Notably, the S of Ag_2Se/MC, PEDOT:PSS@Ag_2Se/MC, and PVP@Ag_2Se/MC films was −129.00 μV/K, −141.95 μV/K, and −147.24 μV/K at 300 K, revealing that the introduction of PEDOT:PSS or PVP could improve the absolute value of S. The $|S|$ of all the films remained almost unchanged in the 300–400 K range, whereas a sharp drop was observed above 400 K, mainly ascribed to the β to α phase transition of Ag_2Se occurring at approximately 407 K[15].

In Fig. 2c, the TE performance for all the films showed significant enhancement compared to their corresponding samples before annealing (Fig. S4), where both σ and $|S|$ were substantially improved, thus yielding a significant enhancement in PF. Notably, the PF of PEDOT:PSS@Ag_2Se/MC and PVP@Ag_2Se/MC films was significantly enhanced compared to that of the Ag_2Se/MC film. A PF of 1634.37 $\mu Wm^{-1} K^{-2}$ at 300 K was achieved for the PVP@Ag_2Se/MC film, and this value increased steadily up to 400 K but sharply declined beyond 400 K due to the abrupt drop in $|S|$. Consequently, the PF of the PVP@Ag_2Se/MC film peaked at 2191.5 $\mu Wm^{-1}K^{-2}$ with the corresponding S of −140.4 μV/K and σ of 1112.4 S/cm at 400 K, positioning it at the forefront of reported flexible Ag-Se-based TE films[9,15,19,21–32] (Fig. S5), and marking the highest value so far among flexible organic/inorganic composite TE films fabricated via the direct-ink printing.

To gain a deeper understanding of the obtained TE properties, an extensive investigation of the underlying carrier transport mechanisms was undertaken. Figure 2d showed the carrier concentration (n_H) and mobility (μ) based on the Hall effect measurement. The PVP@Ag_2Se/MC film exhibited the highest n_H when compared with Ag_2Se/MC and PEDOT:PSS@Ag_2Se/MC films. This might be attributed to the existence of more interstitial Ag[27], which ultimately contributed to the highest σ ($\sigma = n_H\mu e$, where e is the electron charge) among all the composite films, although its μ was moderately reduced.

Interestingly, the $|S|$ of the PVP@Ag_2Se/MC film was higher than those of the other films at 300 K. For semiconductors, the S was typically proportional to the effective mass (m^*) of the charge carriers and inversely proportional to $(n_H)^{2/3}$, as described by the Eq. (1):

$$S = \frac{8\pi^2 k_B^2}{3eh^2} m^* T \left(\frac{\pi}{3n_H}\right)^{2/3} \quad (1)$$

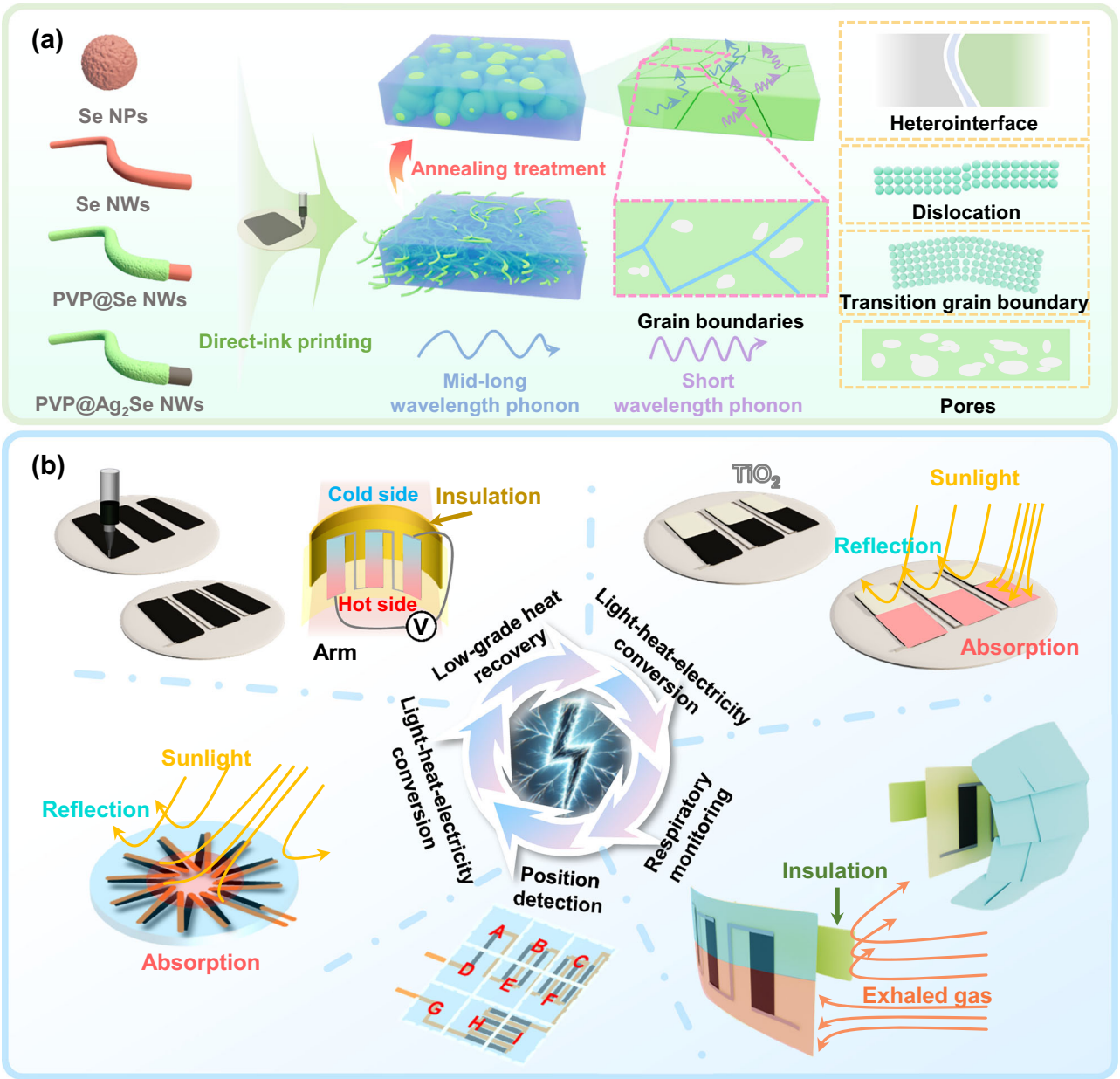

Fig. 1 | Conceptual design of TE films and f-TEGs. Schematic diagrams showing the fabrication of **a** PVP@Ag_2Se/MC films with intriguing phase interfaces, lattice defects, etc., and **b** f-TEGs for multi-scenario applications.

Here, h, k_B, and e denote the Planck's constant, Boltzmann constant, and electron charge[33,34]. Figure 2e showed the corresponding Pisarenko plots of $|S|$ versus n_H. The simulation based on the single parabolic band (SPB) model was detailed in the Supplementary Information Note S3. When compared with the other films, the higher n_H in the PVP@Ag_2Se/MC film at 300 K commonly led to a lower $|S|$, while this effect was offset by the substantial enhancement in m^* from 0.17 m_e to 0.24 m_e (m_e is the electron mass), ultimately resulting in a slight increase in $|S|$ at 300 K.

Figure 2f showed the temperature-dependent n_H and μ of the PVP@Ag_2Se/MC film. The n_H and μ were 4.55×10^{18} cm^{-3} and 1032.40 $cm^2V^{-1}s^{-1}$ at 300 K, respectively. The n_H decreased moderately before 340 K and then increased rapidly from 340 K to 420 K. The μ increased quickly before 340 K and then remained stable until 400 K, followed by a slight decline between 400 K and 420 K. Thus, the n_H and μ jointly determined the gradually increasing trend of its σ with temperature rising.

Under the assumption of homogeneous grain size and distribution in a crystal, the μ can be given as follows[35]:

$$\mu = Le\left(\frac{1}{2\pi m^* k_B T}\right)^{1/2} exp\left(-\frac{E_B}{k_B T}\right) \quad (2)$$

Here, L denotes the average crystallite size, and the temperature-dependent m^* of the PVP@Ag_2Se/MC film calculated based on the SPB model was illustrated in Fig. S6. The relationship between $\ln(\mu(m^*T)^{1/2})$ and $(k_BT)^{-1}$ was shown in Fig. 2g, and notably, the $\ln(\mu(m^*T)^{1/2})$ showed an obvious turning point above 400 K, which might be ascribed to the β to α phase transition of Ag_2Se occurring at approximately 407 K. Compared with other reported Ag_2Se-based composite films[9,15,16,36,37], the PVP@Ag_2Se/MC film in our work exhibited a relatively high PF of 2191.5 $\mu Wm^{-1}K^{-2}$ at 400 K, with a n_H of 5.26×10^{18} cm^{-3} (Fig. 2h).

The determination of in-plane κ in the polymer-based TE composite films remains challenging, particularly for composite films on

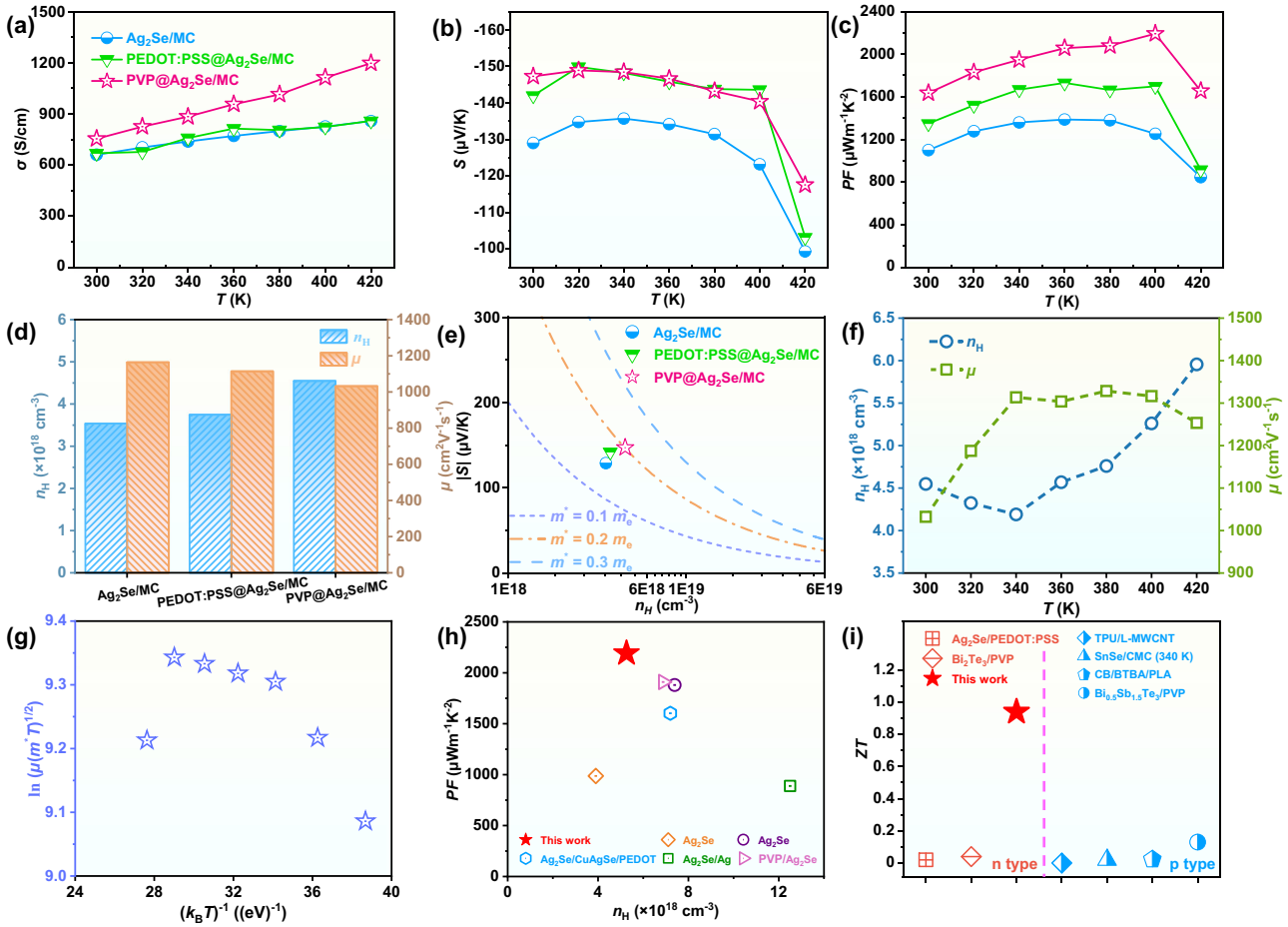

Fig. 2 | Evaluation of TE properties and modeling analysis. a σ, **b** S, and **c** PF versus temperatures (300–420 K) for the Ag_2Se/MC, PEDOT:PSS@Ag_2Se/MC, and PVP@Ag_2Se/MC films. **d** n_H & μ for the composite films at 300 K. **e** Pisarenko plots of $|S|$ versus n_H for the composite films at 300 K. **f** Temperature-dependent n_H & μ (300–420 K), and **g** $\ln(\mu(m^*T)^{1/2})$ versus $(k_BT)^{-1}$ for the PVP@Ag_2Se/MC film. **h** PF versus n_H of PVP@Ag_2Se/MC film compared with reported Ag_2Se based films[9,15,16,36,37], and **i** ZT value of PVP@Ag_2Se/MC film compared with reported flexible organic/inorganic composite films prepared via 3D printing[43–47] (TPU thermoplastic polyurethane, L-MWCNT long multiwalled carbon nanotube, CMC carboxymethyl cellulose, CB carbon black, BTBA Bi_2Te_3 based alloy, PLA polylactic acid).

flexible substrates[38]. Herein, both theoretical calculation and experimental measurement were conducted to evaluate the in-plane κ of PVP@Ag_2Se/MC film. First, the calculated in-plane κ of 0.36–0.56 $Wm^{-1}K^{-1}$ for the PVP@Ag_2Se/MC film was obtained using the reference-outlined series-parallel connected model[39], and the calculation method was also described in the Supplementary Information Note S4. Subsequently, the in-plane κ of ~ 0.52 $Wm^{-1}K^{-1}$ at 300 K for the PVP@Ag_2Se/MC film was measured using the 3ω method (Supplementary Information Note S5 and Fig. S7), and this value aligned well with the above-mentioned theoretical calculations. Such low κ could be attributed to several factors: (1) the pristine Ag_2Se has a low κ of ~ 0.6–1.0 $Wm^{-1}K^{-1}$[19,40]; (2) the PVP and MC, as typical polymers, have inherently low κ[41,42]; and (3) the pores, interfaces, and defects could effectively scatter the phonons (discussed later). Ultimately, the corresponding ZT of the PVP@Ag_2Se/MC film was 0.94 at 300 K, which represented the highest reported value among all the flexible organic/inorganic composite films prepared via 3D printing[43–47] (Fig. 2i).

Comprehensive characterizations to understand the obtained high thermoelectric performance

A series of comprehensive characterizations and in-depth analyses were conducted to investigate the factors responsible for the exceptional TE properties of the PVP@Ag_2Se/MC film. The XRD patterns revealed that the pure Ag_2Se phase existed in the Ag_2Se/MC, PEDOT:PSS@Ag_2Se/MC, and PVP@Ag_2Se/MC films (Fig. S8), while the peaks of PEDOT:PSS, PVP, and MC were not detected, which might be related to the poor crystallinity and/or low content of the polymers[20,48]. Moreover, when compared with the as-synthesized Ag_2Se NWs, PEDOT:PSS@Ag_2Se NWs, and PVP@Ag_2Se NWs, the intensities of the (112) and (121) peaks of Ag_2Se in the Ag_2Se/MC, PEDOT:PSS@Ag_2Se/MC, and PVP@Ag_2Se/MC films significantly decreased, whereas those of (002), (004), (013), and (014) became much stronger. The results suggested that the as-prepared films were highly oriented along (00 l) and (01 l) after the cold pressing and annealing process, which was beneficial for enhancing the TE properties of Ag_2Se[49].

The SEM images of all nanowires revealed one-dimensional structures, and the morphology of PEDOT:PSS@Ag_2Se NWs exhibited some differences compared to those of the other nanowires (Figs. 3a and S9). Typical TEM images (Figs. 3b and S10) indicated that the PVP and PEDOT:PSS were successfully coated on the surfaces of Ag_2Se NWs. For instance, a clear interface between the amorphous region (thickness ~ 10 nm, Fig. 3b) and the Ag_2Se can be observed in the PVP@Ag_2Se NWs (Fig. 3c).

Figures S11 and 12 showed SEM images of Ag_2Se/MC, PEDOT:PSS@Ag_2Se/MC, and PVP@Ag_2Se/MC films before and after the annealing process, respectively. After annealing, the morphologies of the three films changed significantly, and the Ag_2Se NWs, PEDOT:PSS@Ag_2Se NWs, and PVP@Ag_2Se NWs underwent sintering to

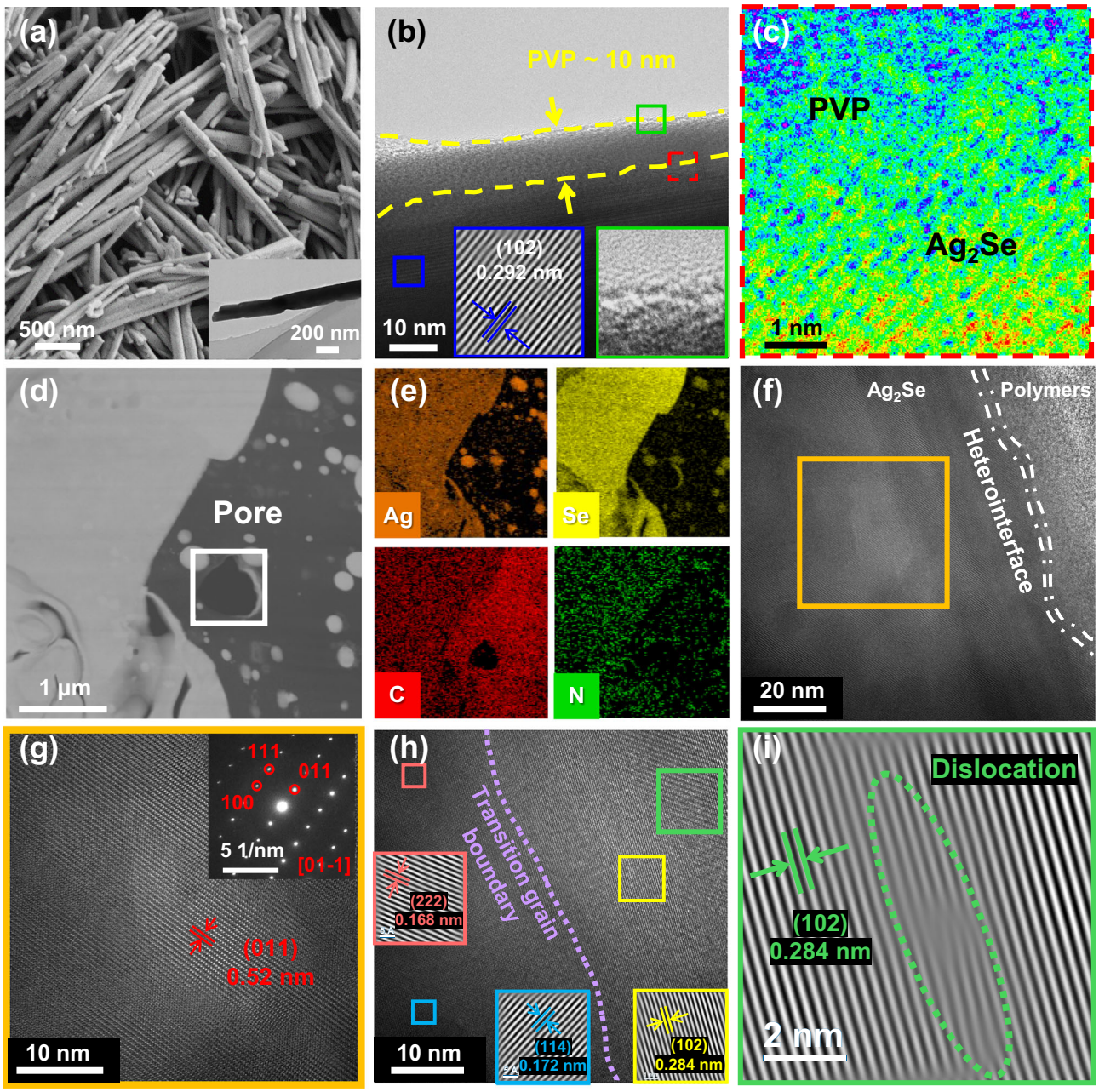

Fig. 3 | Electron microscopy analysis to understand the achieved high TE performance. a SEM image and TEM image (the inset) of PVP@Ag_2Se NWs. **b** HRTEM image of PVP@Ag_2Se NWs. The insets show the inverse fast Fourier transform image derived from the blue-framed area, and the enlarged green area for the PVP@Ag_2Se NWs. **c** The enlarged red-framed area in (**b**). **d** HAADF-STEM image of PVP@Ag_2Se/MC film, and **e** EDS mappings of Ag, Se, C, and N elements. **f** HRTEM image of PVP@Ag_2Se/MC film with a typical heterointerface. **g** The enlarged orange-framed area in (**f**), with the inset showing the corresponding SAED patterns. **h** HRTEM image of PVP@Ag_2Se/MC film showing a transition grain boundary. **i** Inverse fast Fourier transform image obtained from (**h**), suggesting typical dislocations.

form conductive networks, which facilitated the carrier transport in the composite films. The Ag_2Se particles on the surface of the PVP@Ag_2Se/MC film caused by sintering were smaller than those of the other composite films, might because PVP acted as a strong capping agent to inhibit the growth of Ag_2Se particles[9,50]. The corresponding EDS mappings of the Ag_2Se/MC, PEDOT:PSS@Ag_2Se/MC, and PVP@Ag_2Se/MC films were shown in Figs. S13–15. The base elements of Ag, Se, C, and O originated from Ag_2Se and MC, and the additional S or N elements were ascribed to PEDOT:PSS or PVP, respectively.

To analyze the internal microstructure of the composite films, lamellar TEM samples were prepared using focused ion beam (FIB) technology. Figure 3d showed the high-angle annular dark field scanning TEM (HAADF-STEM) image of PVP@Ag_2Se/MC film. Small pores (e.g. white square in Fig. 3d) were observed in PVP@Ag_2Se/MC film, likely due to the incomplete decomposition of MC (thermogravimetric analysis as shown in Fig. S16) and sintering of Ag_2Se NWs. The pores can further enhance phonon scattering, so as to reduce the κ of the film. Figure 3e displayed the EDS mappings corresponding to the area shown in Fig. 3d, and the distribution of N was consistent with that of Ag and Se, mainly due to the surfaces of Ag_2Se NWs being coated with PVP.

High-resolution TEM (HRTEM) images of Ag_2Se grains in PVP@Ag_2Se/MC film were shown in Fig. 3f, g, which exhibited high crystallinity. A clear heterointerface was observed between Ag_2Se and

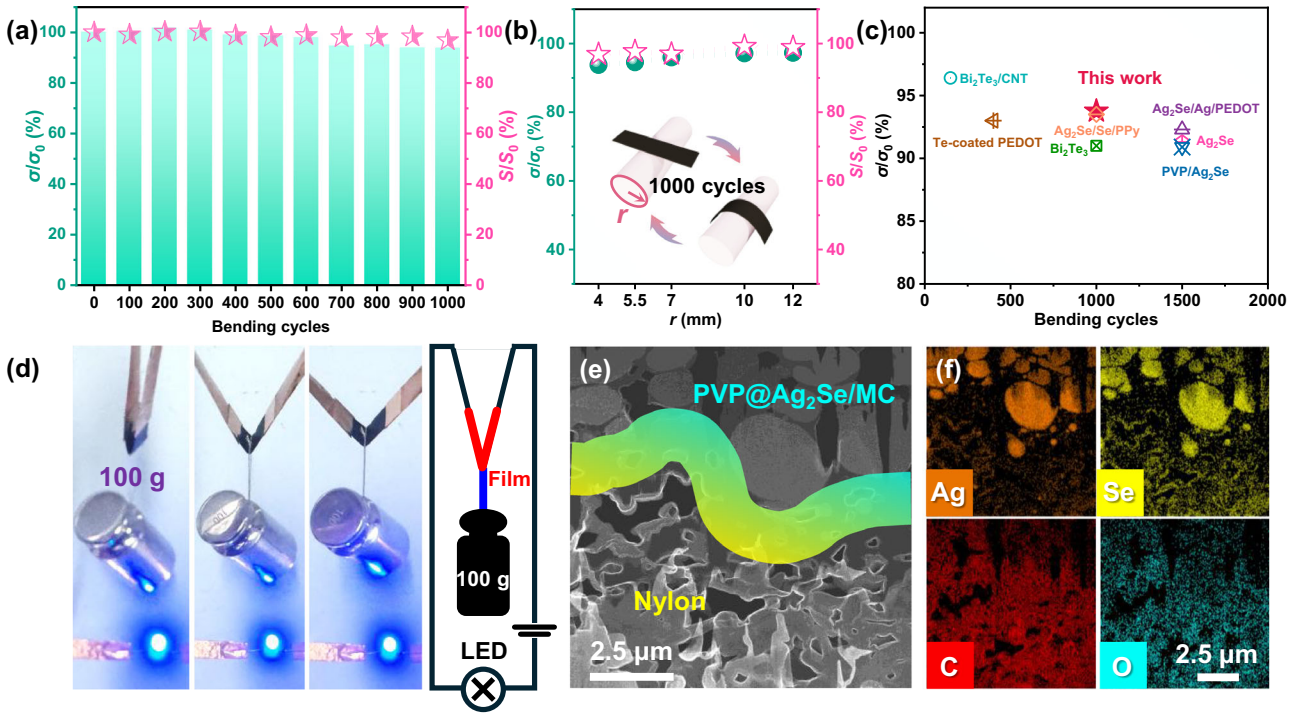

Fig. 4 | Examination of flexibility. a σ/σ_0 and S/S_0 of PVP@Ag_2Se/MC film versus bending cycles at $r = 4$ mm. **b** σ/σ_0 and S/S_0 of the PVP@Ag_2Se/MC film after 1000 bending cycles at $r = 4$, 5.5, 7, 10, and 12 mm. **c** Flexibility comparison of PVP@Ag_2Se/MC film and other reported flexible TE materials[16,18,21,51–54] (CNT carbon nanotube, PPy polypyrrole, PEDOT poly(3,4-ethylenedioxythiophene)). **d** Digital photographs of the PVP@Ag_2Se/MC film lifting a 100 g weight and serving as a flexible conductor with a corresponding circuit diagram. **e** HAADF-STEM image showing the interfacial bonding between the PVP@Ag_2Se/MC film and nylon membrane, and **f** corresponding EDS mappings of Ag, Se, C, and O elements.

polymer (Fig. 3f). Figure 3g displayed the enlarged orange square in Fig. 3f, and typically the (011) crystal plane of Ag_2Se can be identified. The inset of Fig. 3g showed its selected area electron diffraction (SAED) pattern, revealing the zone axis is along the [01-1]. A transition grain boundary (purple dashed line) and a typical dislocation (green dashed circle) were observed in the HRTEM images of the PVP@Ag_2Se/MC film in Fig. 3h, i, respectively. Such well-crystallized grains facilitated carrier transport, while transition grain boundaries and typical dislocations were beneficial for scattering phonons.

Overall, the comprehensive TEM analysis suggested that the excellent TE performance of PVP@Ag_2Se/MC films arose from several key factors: (1) PVP coating effectively reduced the grain size and introduced more interfaces, favoring the formation of interstitial Ag, thereby significantly increasing the n_H and σ; (2) The formed hetero-interfaces enhanced carrier scattering, so as to increase the $|S|$; and (3) The formed pores, transition grain boundaries, and dislocations were beneficial for scattering phonons and then decreasing the κ.

Evaluation of flexibility

Flexibility is crucial for practical applications, in addition to excellent TE performance. Figure 4a showed the changes of σ and S versus bending cycles for the PVP@Ag_2Se/MC film at a $r = 4$ mm. After 1000 bending cycles, the σ and S remained ~ 93.76% and ~ 96.85% of the corresponding initial values (σ_0 and S_0), and the σ/σ_0 and S/S_0 exhibited minimal variation after 1000 bending cycles at larger r values (5.5, 7, 10, and 12 mm) (Fig. 4b). The results suggested that the PVP@Ag_2Se/MC film had excellent flexibility and stability, positioning it at the forefront of reported TE films[16,18,21,51–54] (Fig. 4c). By lifting a 100 g weight, the PVP@Ag_2Se/MC film maintained good electrical connectivity even when subjected to different folding angles (Fig. 4d). The above demonstration confirmed the excellent flexibility of the PVP@Ag_2Se/MC films, primarily ascribed to (1) the inherent flexibility of the organic binder MC, as-coated PVP, and nylon membrane, (2) the porous network inside the film formed by the incomplete decomposition of MC and sintering of Ag_2Se NWs, and (3) the tight interfacial bonding between the nylon membrane and PVP@Ag_2Se/MC film (as illustrated in Fig. 4e, f).

3-leg PVP@Ag_2Se/MC f-TEG fabricated via direct-ink printing

The traditional f-TEG fabrication processes involve cutting the composite film into TE legs and then assembling them on a substrate, while using the direct-ink printing, a 3-leg f-TEG prototype can be directly printed from the PVP@Ag_2Se/MC slurry (see details in Fig. 5a and Supplementary Information Note S1) and the corresponding temperature-dependent TE parameters of the composite film after annealing at 250 °C for 1 h were shown in Fig. S17. Figure 5b displayed the variation of open-circuit voltage (V_{oc}) with respect to the temperature difference (ΔT). The V_{oc} can be calculated based on the Eq. (3):

$$V_{oc} = N \cdot |S| \cdot \Delta T \tag{3}$$

Herein, N denotes the number of the TE legs ($N = 3$) and S equals −145.47 μV/K at 300 K. The calculated V_{oc} of PVP@Ag_2Se/MC film and silver paste (the S of silver paste was ~ 1.76 μV/K at 300 K) was 15.75 mV and 0.19 mV at $\Delta T = 36.1$ K, respectively. As a result, the theoretical V_{oc} of the printed f-TEG can be calculated as 15.94 mV (the V_{oc} of PVP@Ag_2Se/MC film plus that of silver paste = 15.75 + 0.19 = 15.94 mV), which was slightly higher than the experimental V_{oc} (15.66 mV), mainly attributed to the unavoidable thermal contact resistance and heat dissipation to the environment[55].

The output power (P) is calculated using the Eq. (4):

$$P = \left(\frac{V_{oc}}{R_{ex} + R_{in}}\right)^2 \times R_{ex} \tag{4}$$

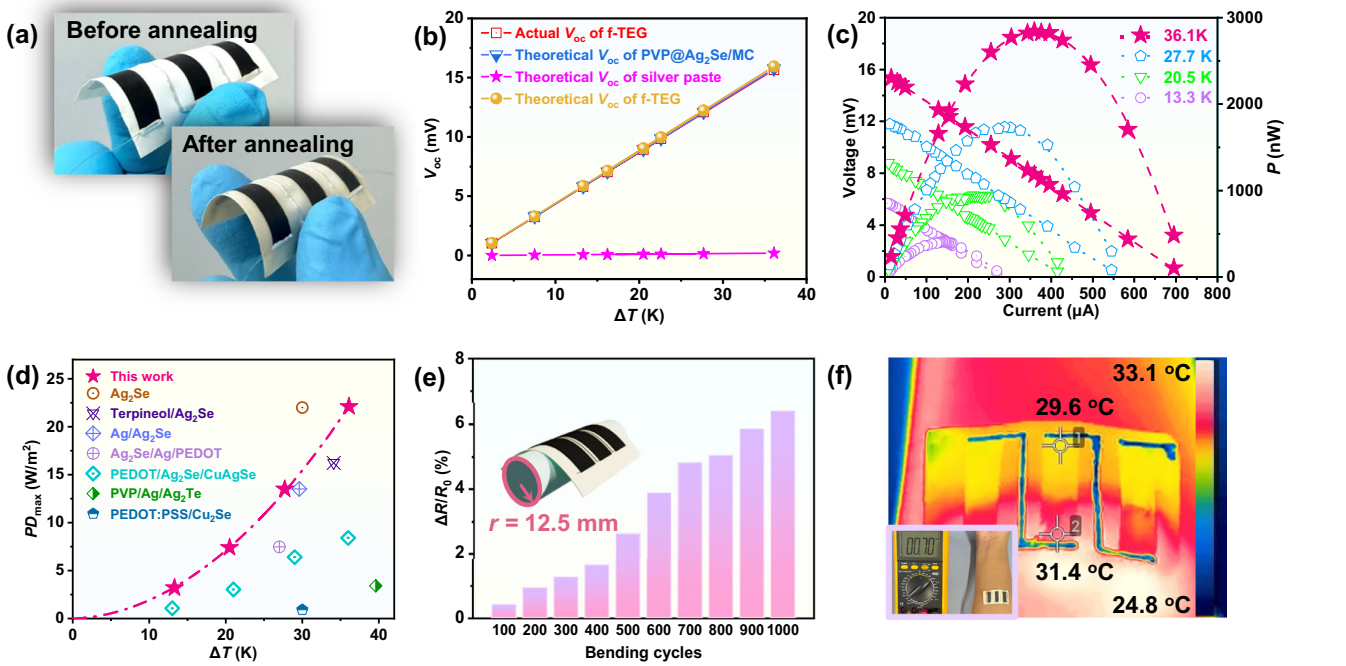

Fig. 5 | Typical printed PVP@Ag_2Se/MC f-TEGs with extraordinary TE performance. a Digital photos of printed 3-leg f-TEG before and after the annealing process. **b** Actual and theoretical results of the relationship between V_{oc} and ΔT. **c** Current-dependent output voltage and P under different ΔT. **d** PD_{max} comparison of the printed PVP@Ag_2Se/MC f-TEG with other typical f-TEGs[16,19,37,53,56–58]. **e** $\Delta R/R_0$ versus bending cycles perpendicular to the TE leg length direction, where the r is 12.5 mm. The inset represents the schematic illustration of the bending measurement. **f** Real-time infrared thermal image of the 3-leg f-TEG (inset showing the f-TEG generated a V_{oc} of 0.70 mV by harvesting the heat dissipated from the human forearm).

where R_{in} is the internal resistance of the f-TEG, and R_{ex} is the external resistance. Figure 5c showed the current-dependent output voltage and P at different ΔT. When $R_{ex} = R_{in}$, the maximal output power (P_{max}) can be obtained, which can be described by Eq. (5):

$$P_{max} = \frac{V_{oc}^2}{4R_{in}} \quad (5)$$

The P_{max} of the f-TEG reached 411.56 nW, 944.67 nW, 1735.49 nW, and 2842.57 nW, under the ΔT of 13.3 K, 20.5 K, 27.7 K, and 36.1 K, respectively. Thus, R_{in} was determined to be ~ 21.3 Ω, which aligned well with the calculated value based on the formula $R = NL/(A\sigma) =$ 20.0 Ω, where L is the effective length, and A denotes the cross-sectional area perpendicular to the length of the TE leg, respectively. The Au contact layer and Ag electrode employed for the connections primarily contributed to the low contact resistance of ~ 1.3 Ω for the f-TEG (see the zoomed-in illustration in Fig. S18). The maximal power density (PD_{max}) is determined by Eq. (6):

$$PD_{max} = \frac{P_{max}}{NA} \quad (6)$$

An impressive maximum PD_{max} of 22.1 W/m² was ultimately obtained when a ΔT of 36.1 K, surpassing that of most reported f-TEGs (Fig. 5d)[16,19,37,53,56–58].

The resistance change ratio versus bending cycles for the directly printed PVP@Ag_2Se/MC f-TEG, with the bending direction perpendicular to the strip length, was demonstrated in Fig. 5e. After 1000 bends at r = 12.5 mm, the resistance change ratio was less than 7%, demonstrating that the f-TEG has excellent flexibility. Moreover, by attaching the two sides of the printed f-TEG to the human forearm and thermal insulator, respectively, a V_{oc} of 0.70 mV was generated at a ΔT of ~ 1.8 K (the corresponding real-time infrared thermal distribution was visualized in Fig. 5f).

Versatile PVP@Ag_2Se/MC f-TEG for multi-scenario applications

In addition to traditional low-grade heat recovery, f-TEGs have also been applied to position identification, light-heat-electricity conversion, and respiratory monitoring. The printed f-TEG was integrated into a mask, and the V_{oc} generated under different breathing conditions was captured for respiratory monitoring (Fig. 6a, c displayed the configuration and photograph of the mask). As illustrated in Fig. 6b, the frequency of V_{oc} fluctuations was significantly higher during rapid breathing than during normal breathing. This type of mask, functioning as a breath monitor, is helpful for patients, especially those suffering from asthma, to assess their health condition.

Furthermore, with the TiO_2 coating, the printed solar-thermoelectric generator (s-TEG, see details in the Supplementary Information Note S1) can convert light into electricity, mainly due to the significant difference in light absorption efficiency for the visible and near-infrared regions between the PVP@Ag_2Se/MC film and TiO_2[39], thereby expanding the applications of f-TEG. The cycling of V_{oc} for the s-TEG versus time under different light intensities was shown in Fig. 6d. The V_{oc} rose rapidly and then trended toward stability with the light on, while its value decreased quickly when the light was turned off. Such a sudden drop in V_{oc} when the light was abruptly turned off also indicated the quick response of the s-TEG. The peak value of V_{oc} rose from ~ 3.0 mV to ~ 9.1 mV, as the light intensity increased from 1 to 3 suns.

Additionally, the printed s-TEG was also tested at 1 pm and 5 pm under natural sunlight and shadow, and the V_{oc} variation over time was illustrated in Fig. 6e. Notably, the values of V_{oc} at 1 pm and 5 pm consistently increased as the exposure time from 0 to 30 s under sunlight, and then immediately exhibited a decreasing tendency when under shadows. Furthermore, the V_{oc} recorded at 5 pm was substantially lower than that at 1 pm (Fig. 6f), mainly because of the lower light intensity at 5 pm compared to that at 1 pm, suggesting the good sensitivity of the s-TEG to light intensity.

As shown in Fig. S19a, the annular s-TEG was also assembled. When a sun visor was applied as shown in Fig. S19b, the uncovered part

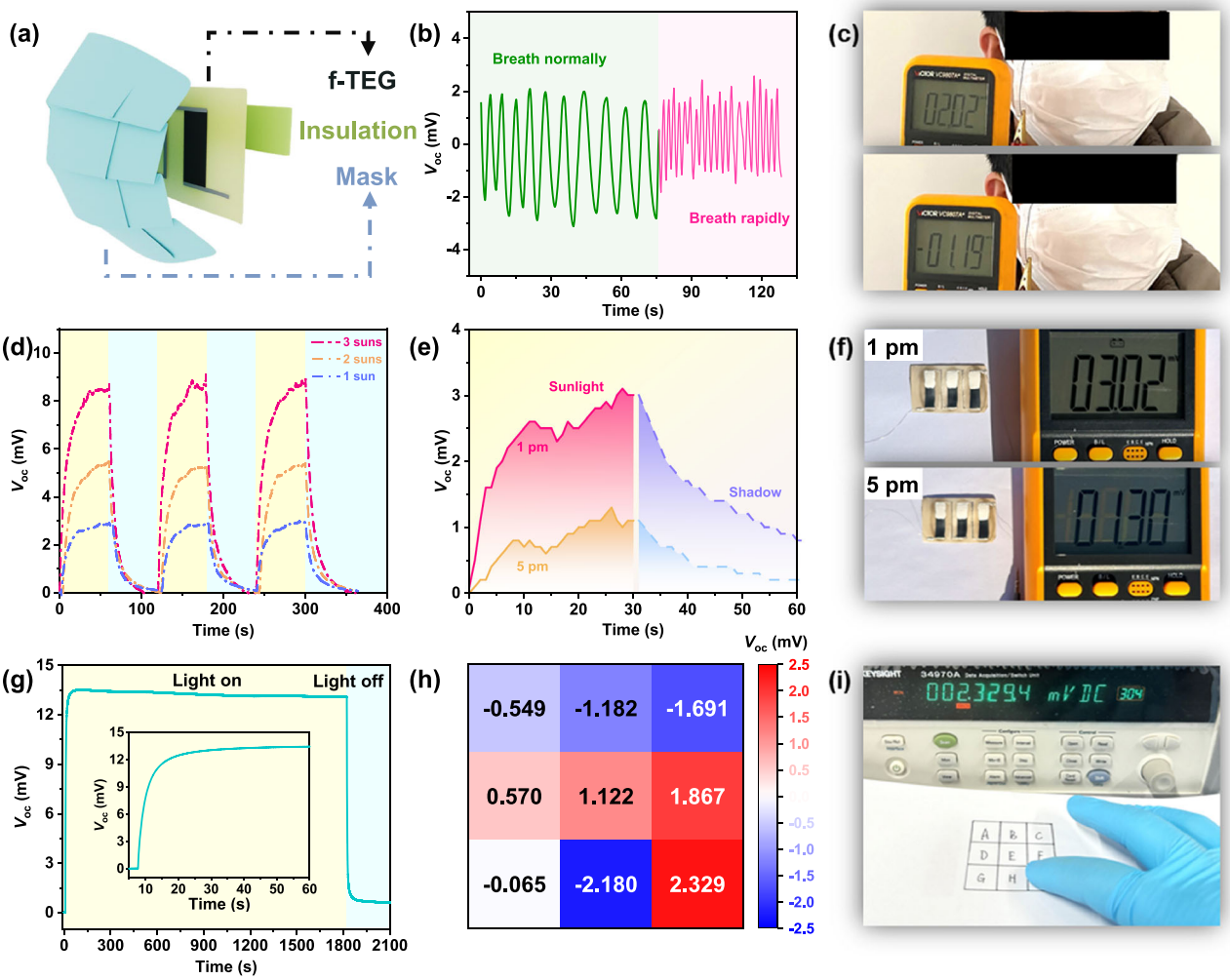

Fig. 6 | Multi-scenario applications of f-TEGs. a The specific structure of the printed f-TEG integrated into a mask for respiratory monitoring. **b** V_{oc} versus time under normal and rapid breathing conditions. **c** Digital photographs of V_{oc} generated during inhalation or exhalation by the f-TEG integrated into the mask. **d** The cycling of V_{oc} for the printed s-TEG versus time under different light intensities of 1 sun, 2 suns, and 3 suns. **e** V_{oc} versus time generated by exposing the printed s-TEG to natural sunlight at 1 pm and 5 pm, and **f** digital photos of V_{oc} yielded by the printed s-TEG. **g** V_{oc} versus time for the as-assembled annular s-TEG. **h** The assembled f-TEG generated a unique V_{oc} when different regions were individually touched by a finger (Fig. S20c), and **i** digital photo showing a V_{oc} ~ 2.33 mV generated when the region I was touched.

of TE legs in the center became the hot side under light, and the corresponding V_{oc} versus time was displayed in Fig. 6g (inset showed the V_{oc} variation in the first 60 s). The V_{oc} retained ~ 97.0% of its maximum value (~ 13.5 mV) after 30 min, illustrating the outstanding stability and energy conversion efficiency of the annular s-TEG. The device structure was optimized to achieve more distinct position identification (Fig. S19c). When the assembled f-TEG was divided into nine parts and a random part was touched with a finger, a unique V_{oc} was generated, as shown in Figs. 6h and S20. For example, a V_{oc} of ~ 2.33 mV was generated when the region I was touched (Fig. 6i). Such a well-defined V_{oc} distribution demonstrates that the f-TEG has a high sensitivity to the placement of the heat source.

Discussion

This study highlights a remarkable advancement in the development of flexible versatile polymer-coated Ag_2Se thermoelectric composite films and devices for multi-scenario applications via a cost-effective direct-ink printing. At 400 K, the PVP@Ag_2Se/MC film reached the peak power factor of 2191.5 $\mu Wm^{-1}K^{-2}$, surpassing all previously reported flexible organic/inorganic composite films fabricated via the direct-ink printing. An effective strategy for improving the TE properties of flexible composite films was developed by introducing heterointerfaces, pores, boundaries, and dislocations through direct-ink printing, cold pressing, and annealing processes. The PVP@Ag_2Se/MC film demonstrated excellent flexibility and stability, retaining 93.76% of its initial electrical conductivity after 1000 bends at $r = 4$ mm. The printed f-TEG achieved a power density of 22.1 W/m^2 at a ΔT of 36.1 K, and its resistance change ratio was less than 7% after 1000 bending cycles at $r = 12.5$ mm. The use of direct-ink printing can enhance the design freedom and manufacturability of f-TEGs, and the printed f-TEGs exhibit huge application potential across multiple scenarios, including low-grade heat recovery, health monitoring, position identification, light-heat-electricity conversion, etc. The direct-ink printing and TE performance optimization strategies for flexible polymer-based films have universal applicability, offering promising solutions for energy harvesting and sensing in wearable electronics.

Methods

Film and device fabrication

Ag_2Se NWs, PEDOT:PSS-coated Ag_2Se NWs, and PVP-coated Ag_2Se NWs were synthesized via wet chemical methods. The corresponding composite films were fabricated on the nylon membranes using the

direct-ink printing. Subsequently, a sequential cold pressing and annealing process was performed to optimize the TE properties. Furthermore, three-leg f-TEGs were printed directly to assess the corresponding application potential across multiple scenarios. The experimental details are provided in the Supplementary Information.

Characterizations and performance measurements

The characterization and measurement details are shown in the Supplementary Information.

Theoretical calculation

The single parabolic band (SPB) model and Pisarenko curves were utilized to analyze the carrier transport performance. Meanwhile, a series-parallel connected model was applied to estimate the in-plane κ. Corresponding details are elaborated in the Supplementary Information.

Data availability

All data supporting the findings of this work are available within the article and Supplementary Information. All data are also available from the corresponding author upon request.

References

1. Kim, J., Campbell, A. S., Avila, B. E. F. & Wang, J. Wearable biosensors for healthcare monitoring. *Nat. Biotechnol.* **37**, 389–406 (2019).
2. Shen, Y. et al. Review on fiber-based thermoelectrics: materials, devices, and textiles. *Adv. Funct. Mater.* **5**, 1105–1140 (2023).
3. Du, Y., Xu, J. Y., Paul, B. & Eklund, P. Flexible thermoelectric materials and devices. *Appl. Mater. Today* **12**, 366–388 (2018).
4. Jia, Y. H. et al. Wearable thermoelectric materials and devices for self-powered electronic systems. *Adv. Mater.* **33**, 2102990 (2021).
5. Yu, D. et al. Volume-metallization 3D-printed polymer composites. *Adv. Mater.* **36**, 2403088 (2024).
6. Qin, Y. X. et al. Grid-plainification enables medium-temperature PbSe thermoelectrics to cool better than Bi_2Te_3. *Science* **383**, 1204–1209 (2024).
7. Huang, J., Liu, X. H. & Du, Y. Highly efficient and wearable thermoelectric composites based on carbon nanotube film/polyaniline. *J. Materiomics* **10**, 173–178 (2023).
8. Kim, G. H., Shao, L., Zhang, K. & Pipe, K. P. Engineered doping of organic semiconductors for enhanced thermoelectric efficiency. *Nat. Mater.* **12**, 719–723 (2013).
9. Jiang, C. et al. Ultrahigh performance polyvinylpyrrolidone/Ag_2Se composite thermoelectric film for flexible energy harvesting. *Nano Energy* **80**, 105488 (2021).
10. Wang, Y. et al. $Bi_{0.5}Sb_{1.5}Te_3$/PEDOT: PSS-based flexible thermoelectric film and device. *Chem. Eng. J.* **397**, 125360 (2020).
11. Karalis, G. et al. A high performance flexible and robust printed thermoelectric generator based on hybridized Te nanowires with PEDOT:PSS. *Appl. Energy* **294**, 117004 (2021).
12. Zhang, L. et al. High-power-density and excellent-flexibility thermoelectric generator based on all-SWCNTs/PVP composites. *Small* **20**, 2306125 (2024).
13. Yang, D. et al. Flexible power generators by Ag_2Se thin films with record-high thermoelectric performance. *Nat. Commun.* **15**, 923 (2024).
14. Liu, M., Zhang, X. Y., Zhang, S. X. & Pei, Y. Z. Ag_2Se as a tougher alternative to n-type Bi_2Te_3 thermoelectrics. *Nat. Commun.* **15**, 6580 (2024).
15. Ding, Y. F. et al. High performance n-type Ag_2Se film on nylon membrane for flexible thermoelectric power generator. *Nat. Commun.* **10**, 841 (2019).
16. Jiang, C. et al. Ultrahigh performance of n-type Ag_2Se films for flexible thermoelectric power generators. *ACS Appl. Mater. Interfaces* **12**, 9646–9655 (2020).
17. Xiao, C. Z. et al. Fabrication of flexible self-supporting black phosphorus nanosheet/PEDOT:PSS thermoelectric composite films by solution 3D printing technology. *Compos. Commun.* **46**, 101815 (2024).
18. Lu, Y. et al. Nanoengineering approach toward ultrahigh power factor Ag_2Se/polyvinylpyrrolidone composite film for flexible thermoelectric generator. *Chem. Eng. J.* **485**, 149793 (2024).
19. Zhang, M. C. et al. Scalable printing high-performance and self-healable Ag_2Se/terpineol nanocomposite film for flexible thermoelectric device. *Energy* **296**, 131232 (2024).
20. Qin, J., Du, Y., Meng, Q. F. & Ke, Q. F. Flexible thermoelectric Cu-Se nanowire/methyl cellulose composite films prepared via screen printing technology. *Compos. Commun.* **38**, 101467 (2023).
21. Li, Y. T. et al. Exceptionally high power factor Ag_2Se/Se/polypyrrole composite films for flexible thermoelectric generators. *Adv. Funct. Mater.* **32**, 2106902 (2021).
22. Zheng, Z. H. et al. Achieving ultrahigh power factor in n-type Ag_2Se thin films by carrier engineering. *Mater. Today Energy* **24**, 100933 (2022).
23. Palaporn, D., Mongkolthanaruk, W., Faungnawakij, K., Kurosaki, K. & Pinitsoontorn, S. Flexible thermoelectric paper and its thermoelectric generator from bacterial cellulose/Ag_2Se nanocomposites. *ACS Appl. Energy Mater.* **5**, 3489–3501 (2022).
24. Wu, M. M. et al. Ultraflexible and high-thermoelectric-performance sulfur-doped Ag_2Se film on nylon for power generators. *ACS Appl. Mater. Interfaces* **14**, 4307–4315 (2022).
25. Kumar, S., Tiadi, M., Trivedi, V., Battabyal, M. & Satapathy, D. K. High-performance selenide-based flexible thermoelectric films. *ACS Appl. Energy Mater.* **6**, 10457–10466 (2023).
26. Liu, Y. et al. Nanoengineering approach toward high power factor Ag_2Se/Se composite films for flexible thermoelectric generators. *ACS Appl. Mater. Interfaces* **15**, 36587–36593 (2023).
27. Hu, Q. X. et al. SWCNTs/Ag_2Se film with superior bending resistance and enhanced thermoelectric performance via in situ compositing. *Chem. Eng. J.* **457**, 141024 (2023).
28. Park, D., Kim, M. & Kim, J. Conductive PEDOT:PSS-based organic/inorganic flexible thermoelectric films and power generators. *Polymers* **13**, 210 (2021).
29. Zhou, K. X. et al. Non-epitaxial pulsed laser deposition of Ag_2Se thermoelectric thin films for near-room temperature applications. *Ceram. Int.* **42**, 12490–12495 (2016).
30. Jindal, S., Singh, S., Saini, G. S. S. & Tripathi, S. K. Optimization of thermoelectric power factor of (013)-oriented Ag_2Se films via thermal annealing. *Mater. Res. Bull.* **145**, 111525 (2022).
31. Zang, J. B. et al. Effect of post-annealing treatment on the thermoelectric properties of Ag_2Se flexible thin film prepared by magnetron sputtering method. *Results Phys.* **45**, 106222 (2023).
32. Hou, S. H. et al. High-performance, thin-film thermoelectric generator with self-healing ability for body-heat harvesting. *Cell Rep. Phys. Sci.* **3**, 101146 (2022).
33. Li, N. H., Zhang, Q., Shi, X. L., Jiang, J. & Chen, Z. G. Silver copper chalcogenide thermoelectrics: advance, controversy, and perspective. *Adv. Mater.* **36**, 2313146 (2024).
34. Gharahcheshmeh, M. H., Dautel, B. & Chowdhury, K. Enhanced carrier mobility and thermoelectric performance by nanostructure engineering of PEDOT thin films fabricated via the OCVD method using $SbCl_5$ oxidant. *Adv. Funct. Mater.* **35**, 2418331 (2024).
35. Shen, J. et al. Enhanced thermoelectric performance in the n-type NbFeSb half-Heusler compound with heavy element Ir doping. *Mater. Today Phys.* **8**, 62–70 (2019).
36. Liu, Y. et al. Fully inkjet-printed Ag_2Se flexible thermoelectric devices for sustainable power generation. *Nat. Commun.* **15**, 2141 (2024).
37. Lu, Y. et al. Ultrahigh performance PEDOT/Ag_2Se/CuAgSe composite film for wearable thermoelectric power generators. *Mater. Today Phys.* **14**, 100223 (2020).

38. Li, X., Cai, K. F., Gao, M. Y., Du, Y. & Shen, S. Recent advances in flexible thermoelectric films and devices. *Nano Energy* **89**, 106309 (2021).
39. Qin, J. et al. Modulating carrier transport by cross-dimensional compositing of Ag_2Se/MXene for high-performance flexible thermoelectrics. *J. Mater. Chem. A* **12**, 17586–17595 (2024).
40. Lee, C., Park, Y. H. & Hashimoto, H. Effect of nonstoichiometry on the thermoelectric properties of a Ag_2Se alloy prepared by a mechanical alloying process. *J. Appl. Phys.* **101**, 24920 (2007).
41. Khan, W. S., Hamadneh, N. N. & Khan, W. A. Prediction of thermal conductivity of polyvinylpyrrolidone (PVP) electrospun nanocomposite fibers using artificial neural network and prey-predator algorithm. *PLoS ONE* **12**, 0183920 (2017).
42. Xie, X. et al. Thermal conductivity, heat capacity, and elastic constants of water-soluble polymers and polymer blends. *Macromolecules* **49**, 972–978 (2016).
43. Burton, M. R. et al. 3D printed SnSe thermoelectric generators with high figure of merit. *Adv. Energy Mater.* **9**, 1900201 (2019).
44. Park, D., Lee, S. & Kim, J. Thermoelectric and mechanical properties of PEDOT:PSS-coated Ag_2Se nanowire composite fabricated via digital light processing based 3D printing. *Compos. Commun.* **30**, 101084 (2022).
45. Chen, B. et al. Flexible thermoelectric generators with inkjet-printed bismuth telluride nanowires and liquid metal contacts. *Nanoscale* **11**, 5222–5230 (2019).
46. Du, Y. et al. Flexible ternary carbon black/Bi_2Te_3 based alloy/polylactic acid thermoelectric composites fabricated by additive manufacturing. *J. Materiomics* **6**, 293–299 (2020).
47. Tzounis, L., Petousis, M., Grammatikos, S. & Vidakis, N. 3D printed thermoelectric polyurethane/multiwalled carbon nanotube nanocomposites: a novel approach towards the fabrication of flexible and stretchable organic thermoelectrics. *Materials* **13**, 2879 (2020).
48. Xu, W. L., Du, Y. & Meng, Q. F. Fabrication of flexible thermoelectric composites by solution 3D printing technology. *Compos. Commun.* **28**, 100944 (2021).
49. Xiao, Z. et al. High-performance Ag_2Se/methyl cellulose thermoelectric composites for flexible power generators. *Energy Mater. Adv.* **5**, 0103 (2024).
50. Baqer, A. A. et al. Effect of polyvinylpyrrolidone on cerium oxide nanoparticle characteristics prepared by a facile heat treatment technique. *Results Phys.* **7**, 611–619 (2017).
51. Lu, Y. et al. Staggered-layer-boosted flexible Bi_2Te_3 films with high thermoelectric performance. *Nat. Nanotechnol.* **18**, 1281–1288 (2023).
52. An, H., Pusko, M., Chun, D., Park, S. & Moon, J. In-situ synthesis of flexible hybrid composite films for improved thermoelectric performance. *Chem. Eng. J.* **357**, 547–558 (2019).
53. Wang, Z. X. et al. High performance Ag_2Se/Ag/PEDOT composite films for wearable thermoelectric power generators. *Mater. Today Phys.* **21**, 100553 (2021).
54. Ni, D., Song, H. J., Chen, Y. X. & Cai, K. F. Significantly enhanced thermoelectric performance of flexible PEDOT nanowire film via coating Te nanostructures. *J. Materiomics* **6**, 364–370 (2020).
55. Liu, X. et al. Free-standing single-walled carbon nanotube/SnSe nanosheet/poly (3, 4-ethylenedioxythiophene): poly (4-styrenesulfonate) nanocomposite films for flexible thermoelectric power generators. *Adv. Eng. Mater.* **22**, 2000605 (2020).
56. Lu, Y. et al. Good performance and flexible PEDOT:PSS/Cu_2Se nanowire thermoelectric composite films. *ACS Appl. Mater. Interfaces* **11**, 12819–12829 (2019).
57. Meng, Q. F. et al. High performance and flexible polyvinylpyrrolidone/Ag/Ag_2Te ternary composite film for thermoelectric power generator. *ACS Appl. Mater. Interfaces* **11**, 33254–33262 (2019).
58. Li, X. et al. Exceptional power factor of flexible Ag/Ag_2Se thermoelectric composite films. *Chem. Eng. J.* **434**, 134739 (2022).

Acknowledgements

This work has been supported by the National Natural Science Foundation of China (52472224), Natural Science Foundation of Shanghai (23ZR1481100), Shuguang Program of Shanghai Education Development Foundation and Shanghai Municipal Education Commission (22SG54). M.H. acknowledges the funding from the Department of Education iLAuNCH Trailblazer and Australian Research Council (FT230100316).

Author contributions

Y.D. and Q.K. conceived the concepts and supervised the project. Y.D., J.Q., M.H., and Q.K. designed the experiments. J.Q. performed the theoretical calculation and experiments. Q.M. assisted with the material characterization and f-TEG output performance measurement. S.C. contributed to the theoretical calculation. M.H. contributed to STEM and microstructural analysis. J.Q., Y.D., and M.H. wrote the draft of the manuscript. All authors participated in data analysis and revised the manuscript.

Competing interests

The authors declare no competing interests.

Additional information

Supplementary information The online version contains supplementary material available at https://doi.org/10.1038/s41467-025-63390-6.

Correspondence and requests for materials should be addressed to Yong Du, Min Hong or Qinfei Ke.

Peer review information *Nature Communications* thanks José Serrano-Claumarchirant, Young Hun Kang, and the other, anonymous, reviewer(s) for their contribution to the peer review of this work. A peer review file is available.